Label-Free Nanoscale ZnO Tetrapod-Based Transducers for Tetracycline Detection

M. Brás[1], J. Zanoni[1], B. P. Falcão[1,2], J. P. Leitão[1], F. M. Costa[1], T. Monteiro[1], S. O. Pereira[1], J. Rodrigues[1]*

[1]i3N, Department of Physics, University of Aveiro, 3810-193 Aveiro, Portugal.
[2]CICECO - Aveiro Institute of Materials, Department of Physics, University of Aveiro, 3810-193 Aveiro, Portugal.

ABSTRACT

Antibiotic pollution of freshwaters and even food products has become an important concern worldwide. Hence, it is of utmost importance to develop cost-effective and reliable devices that can provide information on the presence of such contaminants to the general population. In the present work, zinc oxide (ZnO) nanotetrapods (NTP) produced via a high yield laser processing approach were used as transducers in a luminescent-based immunosensor to detect tetracycline (TC). These tetrapodal structures present needle-shaped branches with a high aspect ratio, exhibiting lengths from hundreds of nanometers to a few micrometers and an average thickness of tens of nanometers, providing a high surface area for bioreceptor immobilization and analyte reaction, which is quite desirable in a transducer material. Besides, these ZnO NTP display intense photoluminescence (PL) at room temperature, making such signal rather promising for transduction. Indeed, the intensity of the ZnO PL signal was seen to correlate with the TC

concentration. The PL quenching with increasing analyte concentration is explained considering the rise in the bending of the electronic bands of the semiconductor near its surface due to increased charge density at this region, induced by the interaction between the bioreceptor (anti-TC antibodies) and the TC molecules. As a larger depletion width (and potential barrier) is promoted near the surface, the excitonic recombination probability is reduced and, consequently, the PL intensity in the ultraviolet spectral region, allowing to use this relationship as sensing mechanism. This information enabled to define a calibration curve for TC quantification in the 0.001 to 1 μg L^{-1} range, which is the range of interest of this antibiotic in freshwaters. A limit of detection (LOD) of ~1.2 ng L^{-1} is reported, corresponding to one of the lowest LOD found in the literature for this antibiotic, indicating that the present ZnO NTP-based biosensors rival current state-of-the-art biosensors.

KEYWORDS: ZnO nanotetrapods; tetracycline; immunosensor; photoluminescence; band bending

1. INTRODUCTION

Over the years, the widespread prescription of antibiotics in the medical and veterinary fields have contributed to the accumulation of these antibacterial drugs in the environment, constituting an important source of pollution [1,2]. Besides its toxic impact on living organisms, antibiotic pollution also indirectly impacts public health, by lowering or even inhibiting the effectiveness of antibacterial drugs [3]. In particular, tetracycline (TC), a broad-spectrum antibiotic usually applied to treat dermatologic pathologies or other bacterial infections [4], can be found in rivers and streams all over the world in concentrations between 0.008 and 1 $\mu g\ L^{-1}$ [2]. Due to the alarming reality brought by antibiotic pollution, several methodologies and devices have been explored over the years in an attempt to achieve simple and fast detection with high selectivity, sensitivity, and reliability, capable of detecting TC in concentrations found in the environment. Nowadays, the most used methods for antibiotic detection are based on analytic processes [5–10]. Although these methods are well established, they require complex sample pre-treatment processes and involve large and expensive instrumentation, as well as trained operators, which makes them confirmatory methods rather than in-situ and real-time tests. Therefore, the development of biosensors is needed for providing simpler, user-friendly and low-cost solutions for accurate detection outcomes. Indeed, these devices have started to be explored for the detection of TC in the last decade. Among them, the most studied are the electrochemical [11–13] and optical ones [14–20], presenting limit of detection (LOD) values as low as ~1 $ng\ L^{-1}$ [13,17,21].

The material chosen to act as transducer in biosensors also plays a fundamental role in their performance. In this context, nanomaterials have received great attention, as they evidence unique properties, such as higher surface area and reactivity, promoting a higher sensitivity to biological targets and enabling a fast detection [22,23]. Among the many that

have been the subject of research, zinc oxide (ZnO), a wide bandgap semiconductor with an energy gap of ~3.3 eV at room temperature (RT) [24], is a promising candidate to be incorporated in optical biosensors due to its luminescence characteristics. It is possible to take advantage of the ZnO radiative recombination for direct optical detection, using the luminescence signal from the transducer without the need for additional fluorophores [25]. Indeed, as the photoluminescence (PL) of ZnO is very sensitive to small modifications at its surface, it is expected to provide high sensitivity to the sensors using this signal for transduction [25,26]. Besides, its low-cost, high yield and simple growth technologies make it a cost-effective and competitive material, which is also an important and appealing factor for its choice as transducer material. Some authors have already reported biosensors based on the luminescence of ZnO nanostructures, where the change of the intensity of different optical centers, in particular the near band edge (NBE) emission, has been correlated with the analyte concentration. Several analytes have been successfully detected by monitoring the changes in the PL intensity of ZnO-based nanostructures, namely glucose [22,27,28], cholesterol [29], *Salmonella* [30], Grapevine virus A-type [31], antibodies (AB) against bovine leukemia virus [32], human leukemic cells [33,34], Ochratoxin A [35] and Aflatoxin B1 [36]. For instance, in the works of Tamashevski et al. [33,34], the detection of human leukemic cells from different cell lines (IM9 [33] and MOLT-4 [34]) was assessed, revealing an increase in the NBE radiative recombination intensity when increasing concentrations of the cells were immobilized onto the surface of the AB-functionalized ZnO nanorods, up to a certain threshold, after which the signal experienced a saturation/stabilization. Likewise, Myndrul et al. [36] also observed an increase in the PL signal with increasing analyte concentration in their Aflatoxin B1 biosensors, followed by the saturation of the signal, likely related to the unavailability of AB to further react with the antigens above a certain concentration [36]. It is worth noting that in that case,

instead of the NBE, the authors monitored the visible band peaked at 565 nm. Our group also reported a PL-based immunosensor for the detection of the human chorionic gonadotropin (hCG) hormone using ZnO tetrapodal nanostructures functionalized with anti-hCG AB [37]. Contrary to the two previously mentioned works, when the hCG was incubated on the sensor's surface, the intensity of the NBE signal decreased as higher concentrations of hCG were added, in line with others works [30,35]. This behavior was attributed to the specific interaction between anti-hCG AB and the hCG hormone by the formation of an immune complex, which has an impact on the ZnO's surface charge and subsequently on the PL intensity [37]. Hence, ZnO has demonstrated interesting potential to be used as a transducer, motivating further exploitation in the detection of other analytes relevant for health and the environment, as is the case of TC. Moreover, using such an optical approach to probe this antibiotic enables interrogating the sensors using light, collecting a signal that is also composed of photons, which can provide remote sensing. This is indeed useful when operating in specific environments, as, the ones where the need for electrical contacts can pose additional concerns/drawbacks (e.g. in water). As well, the simplicity of the probing method, as this is a label-free detection, and the signal collection are other advantages of the present approach [36].

In the present work, ZnO nanotetrapods (NTP) produced by laser-assisted flow deposition (LAFD) were used to form the transducer layer of the luminescent-based biosensors, in which anti-TC AB were immobilized via covalent binding to act as the bioreceptors for TC detection. Such tetrapod morphology, with branches with an high aspect ratio provide a higher number of surface adsorption sites, which is expected to enhance the sensitivity of the sensors [36]. The surface functionalization process was monitored by Fourier transform infrared (FTIR), photoluminescence (PL), and PL excitation (PLE) spectroscopies and the detection was carried out by the analysis of the ZnO PL intensity

signal for each TC concentration. The results revealed a linear decrease in the intensity of the near band edge (NBE) transitions with the increase in the TC concentration in a logarithmic scale and in the range between 0.001 and 1 μg L^{-1}, which is well within the range of interest for detection of TC in rivers and streams.

2. EXPERIMENTAL DETAILS

2.1 MATERIALS' PREPARATION AND FUNCTIONALIZATION

ZnO NTP were prepared via a thermal evaporation based method designated by LAFD (step 1 in Figure 1), as described elsewhere [38]. Briefly, a highly focused CO_2 laser (λ=10.6 μm) is used as a heating source to promote the thermal decomposition of a ZnO precursor, which is composed of a commercial ZnO powder (from AnalaR, 99.7%) mixed with polyvinyl alcohol (PVA, 0.1 g mL^{-1}, Merck) and extruded into cylindrical rods. These rods are then attached to a spindle present inside the growth chamber, which enables the movement of the precursor towards the laser incidence, as well as its rotation during the synthesis, promoting a more homogeneous deposition on the substrate/holder. In the present work, a power of 60 W was applied, leading to the formation of a tetrapodal (TP) morphology (see Figure 2). More details regarding the morphological and structural properties of these ZnO NTP can be found in previous works [37,38]. Nevertheless, we would like to stress out that under such growth conditions, the NTP typically exhibit needle-shaped branches with lengths in the range of hundreds of nanometers and thickness decreasing from the central region to the tip of the branch, with only a few tens of nanometers in the wider (central) region (Figure 2a).

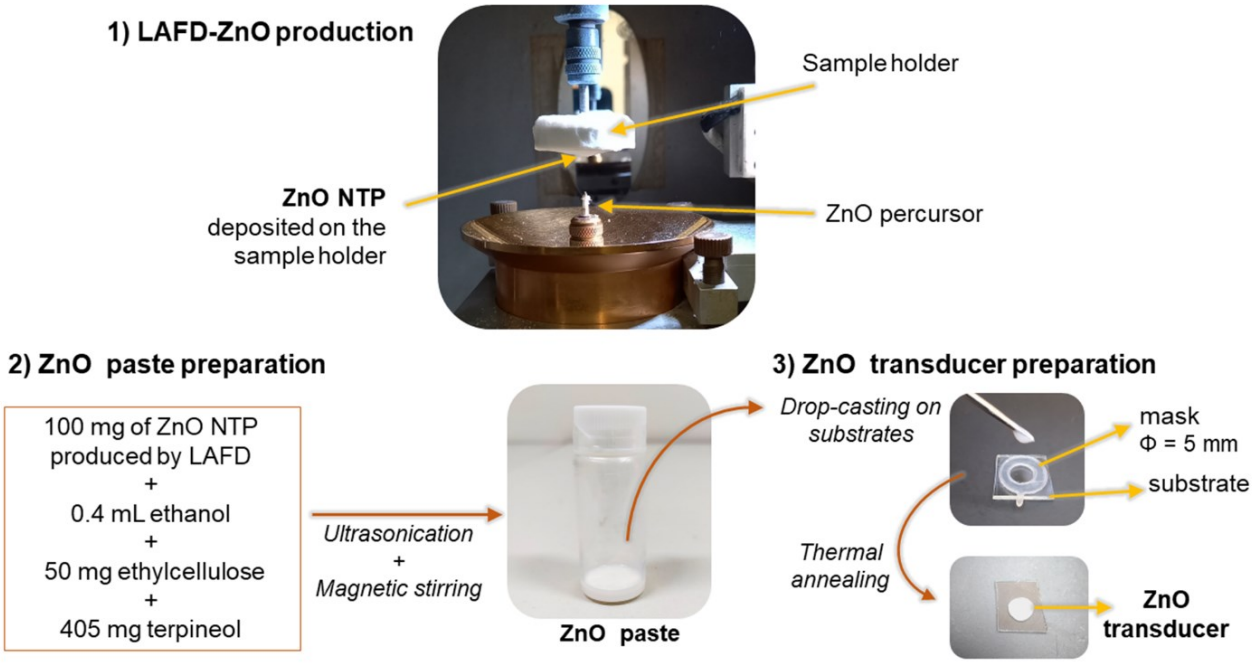

Figure 1. Schematic illustration of the steps involved in the preparation of the ZnO transducers: 1) LAFD production of ZnO, 2) paste preparation, and 3) ZnO transducer preparation.

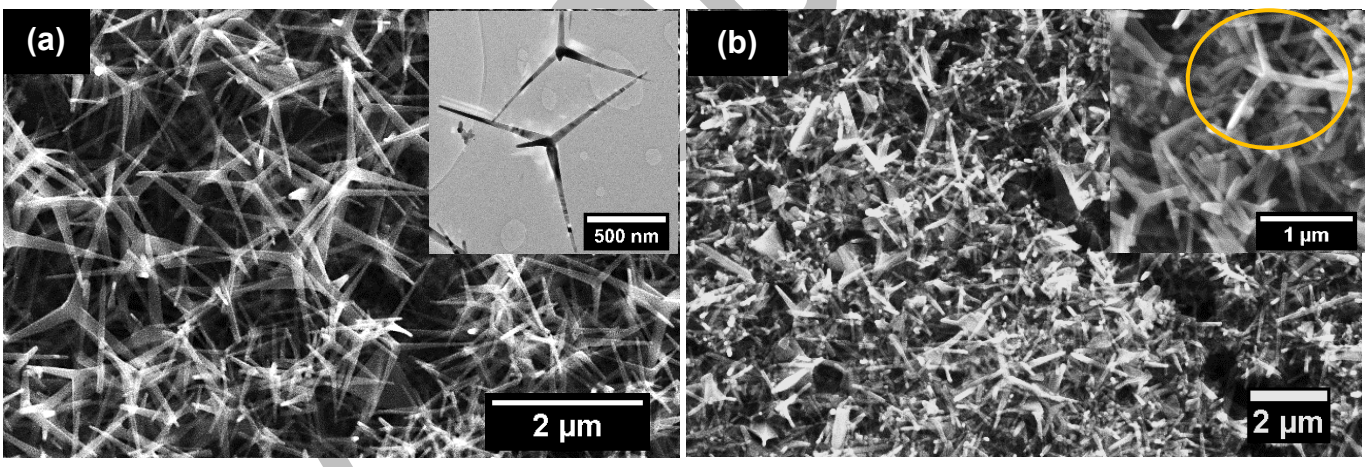

Figure 2. Representative SEM images of the (a) as-produced ZnO NTP and (b) transducer surface after deposition and thermal annealing. Insets: (a) transmission electron microscopy image showing two ZnO NTP; (b) higher magnification SEM image of the transducer surface, highlighting that the tetrapod morphology is kept after deposition and thermal annealing.

The ZnO NTP obtained by LAFD were thereafter collected and 100 mg of this powder was mixed with 0.4 mL of ethanol (absolute, analytical reagent grade, Fisher Chemical), 50 mg of ethylcellulose (Sigma-Aldrich), and 405 mg of terpineol ($C_{10}H_{18}O$, Sigma-Aldrich), resulting in a paste (step 2 in Figure 1) that facilitates the deposition of the ZnO NTP onto fluorine-doped tin oxide (FTO)-coated glass substrates. The deposition of the ZnO paste is done over a circular shaped mask with a 5 mm diameter (step 3 in Figure 1), guaranteeing that all samples had approximately the same volume and area of deposited ZnO. These platforms were pre-dried at RT, under atmospheric conditions and then subjected to a thermal annealing process. For that purpose, the samples were placed inside an oven for 10 minutes at 100 ºC, followed by an additional 30 min at 400 ºC, with a heating rate of 5 ºC min^{-1}. The obtained structures were subsequently used as the transducer layer of the developed biosensor. Hence, after the deposition and the thermal treatment, the transducer is comprised of a highly porous 3D network of ZnO NTP (Figure 2b), exhibiting a high surface area accessible for the biorecognition element to be immobilized and with an easy permeability for the analytes to react, as reported/discussed elsewhere [37,39,40]. It is important to stress out that neither morphological nor structural changes are observed after the transducer formation (deposition and thermal annealing), apart from the presence of some loose branches that detached from the tetrapod structure during the magnetic stirring step of the paste preparation process [40]. As an additional note, it is worth mentioning that the FTO-coated glass acts simply as substrate/mechanical support of the ZnO nanostructures, as no electrical bias is necessary for the here presented optical measurements.

The surface functionalization of the transducers (see a schematic representation of the process in Figure 3), which aims to immobilize the biorecognition element, tetracycline polyclonal antibody (anti-TC antibodies, PA1-75450, from Invitrogen), was

accomplished via covalent immobilization. In this process, 10 µL of (3-aminopropyl)triethoxysilane (APTES, ≥ 98%, from Sigma-Aldrich) were added in a mixture of ethanol and deionized (DI) water (70:30 %v/v), producing a 1%v/v APTES solution. A 50 µL drop of this solution was deposited on the surface of the ZnO transducers and left for 1 h in a humid atmosphere. After this time, the samples were rinsed with DI water and placed in an oven for 20 minutes at 120 ºC, thereby creating ZnO-APTES samples. In the next step, 12.5 µL of *N*-(3-dimethylaminopropyl)-*N'*-ethylcarbodiimide hydrochloride (EDC, 0.1 M, from Sigma-Aldrich) was mixed with 12.5 µL of *N*-Hydroxysuccinimide (NHS, 0.25 M, from Sigma-Aldrich) and 25 µL of anti-TC AB diluted to a concentration of 0.5 mg mL^{-1} in physiological solution (PS, 0.137 M sodium chloride (NaCl, Sigma-Aldrich) and 0.027 M potassium chloride (KCl, Sigma-Aldrich) at pH=5.8). A 50 µL drop of this fresh solution was deposited on the ZnO-APTES surface and incubated for 2 h in a humid atmosphere at ~ 10 ºC. Then, the samples were rinsed with PS, originating the ZnO-APTES-AB samples. The last step in the preparation of the sensor was the deposition of 50 µL of bovine serum albumin (BSA, 10 µg ml^{-1}, Alfa Aesar, prepared in PS) on the surface of the previous samples, which was then incubated for another 2 h in order to passivate the surface, thus minimizing nonspecific interactions between the analyte and the ZnO surface. These samples were again rinsed with PS, resulting in the sensor samples ZnO-APTES-AB-BSA.

Samples functionalized only with BSA (ZnO-APTES-BSA, without any antibody) were also prepared in order to act as control samples in the detection measurements.

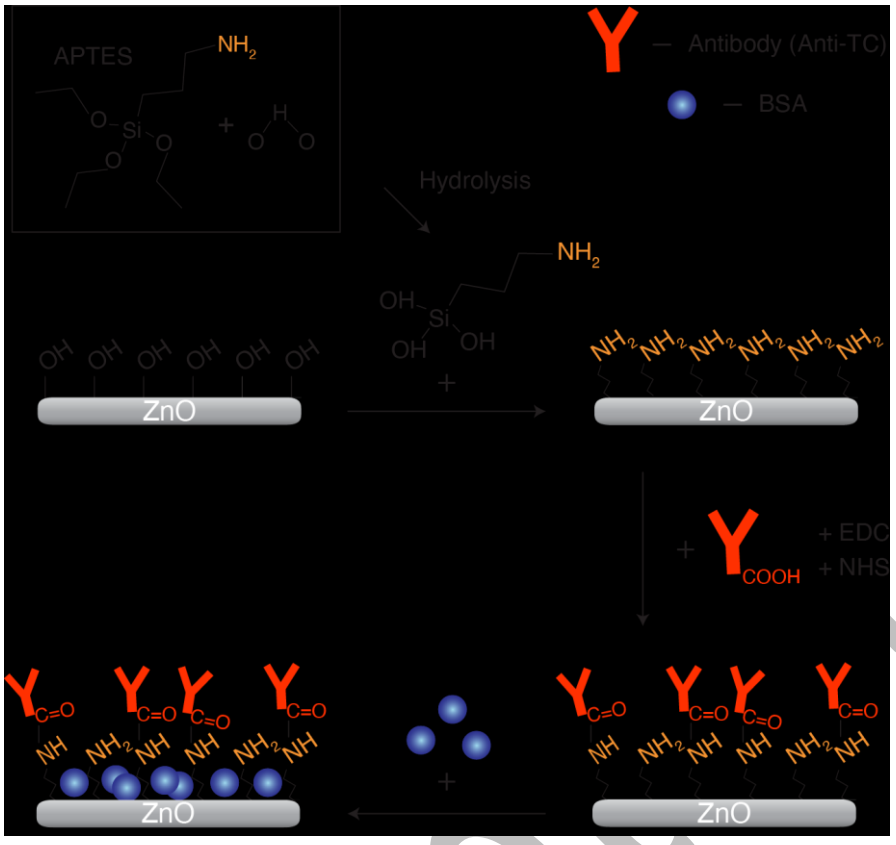

Figure 3. Schematic representation of the procedure followed for covalent immobilization of the bioreceptor onto the transducer platforms.

2.2 MATERIALS' CHARACTERIZATION

Infrared absorption measurements were performed on a Bruker Vertex 80v FTIR spectrometer equipped with a Hypherion microscope unit to evaluate the presence of surface functional groups. Data were collected at RT and ambient conditions in the backscattering reflectance mode using a liquid N_2-cooled MCT detector (D316, Bruker) and a ×15 objective lens. All spectra were compensated for atmospheric gases (H_2O and CO_2) and the baseline was corrected using the concave rubberband method. A piece of Al-coated glass was used to collect the background spectrum. FTIR data were acquired for each step of the functionalization process.

Additional optical properties of the produced materials were evaluated at RT by steady-state PL and PLE. The measurements were conducted in a Fluorolog-3 Horiba Scientific

set-up with a double additive grating Gemini 180 monochromator (1200 grooves mm^{-1} and 2×180 mm of optical path) in the excitation and a triple grating iHR550 spectrometer in the emission (1200 grooves mm^{-1} and 550 mm), under the incidence of a 450 W Xenon lamp, where the excitation wavelength was set to 325 nm in all the PL studies. The PLE was measured by setting the detection monochromator at the maxima of the emission that one wanted to probe and the emission intensity was registered as the excitation was scanned to higher energies. The functionalization procedure was also monitored in each step by both PL and PLE. All PL and PLE spectra were corrected to the optical response of the measurement system.

2.3 SENSING EVALUATION VIA PL

To evaluate the sensing response of the prepared sensors, several solutions with different TC concentrations were prepared through successive dilutions in PS from an initial TC solution with 270 mg L^{-1} (TC powder, 98.0-102.0% HPLC, from Sigma-Aldrich). Therefore, concentrations from 0.001 to 500 µg L^{-1} were prepared and tested, as detailed in Table 1.

The sensing experiments were conducted by placing 50 µL of a TC solution onto the surface of the sensors and left to incubate for 30 min. After this incubation period, the samples were rinsed with PS to remove the excess of TC that have not specifically bound to the anti-TC AB and were dried in air for 5 min. The PL signal of such samples was measured afterwards. This process was repeated for each TC solution, starting with a sample incubated only in PS, which corresponded to the blank/reference (0 µg L^{-1}) and followed by the TC solutions, from the lowest to the highest concentration. [32,33,35,37]. As so, in this work, the response of the sensor is defined as

$$Response = \frac{{I_{UV}}^0 - {I_{UV}}^{TC}}{{I_{UV}}^0}, \quad \text{Eq. 1}$$

where ${I_{UV}}^0$ corresponds to the integrated intensity of the NBE emission prior to analyte immobilization (0 µg L^{-1}) and ${I_{UV}}^{TC}$ is the integrated intensity of the same emission in the same sample in the presence of a certain analyte concentration.

To infer about the sensor's effective sensing ability and to assure that non-specific interactions between the transducer and the analyte were not taking place, control samples prepared without the specific bioreceptor were also submitted to the same procedure and the results compared to the ones of the sensors. Additionally, one ZnO-APTES-AB-BSA sample was repeatedly incubated (5 times) with a PS solution to evaluate its stability during successive incubation steps. Two additional samples were incubated with ciprofloxaxin (CF powder, ≥ 98% HPLC, from Sigma-Aldrich), under the same concentrations tested for TC, to determine the sensing behavior using another antibiotic that is also frequently present in stream waters, and for which the sensors were not specific (interferent). Finally, two sensors were also tested with TC concentrations from 0.001 to 5 µg L^{-1} mixed with a fixed concentration of CF (0.5 µg L^{-1}) to infer the response of the sensors in the presence of an interferent.

Table 1. Summary of the produced samples, respective functionalization and the analyte concentration used in sensing experiments.

Type of sample	Samples labelling	Functionalization	TC analyte	CF interferent	Concentrations tested (μg L^{-1})	Observations
Sensors	*TC#1 to #4*	APTES-AB-BSA	yes	no	0.01, 0.1, 1, 10, 50, 100 and 500	-
	TC#5 to #11				0.001, 0.01, 0.05, 0.1, 0.5, 1 and 5	-
	TC_CF#12,13			yes	0.001, 0.01, 0.05, 0.1, 0.5, 1 and 5	Fixed CF concentration of 0.5 μg L^{-1}
Controls	*C#1,2*	APTES-BSA		no	0.01, 0.1, 1, 10, 50, 100 and 500	-
	C#3	APTES-AB-BSA	no		-	Incubated 5 consecutive times only with PS
	C#4,5			yes	0.001, 0.01, 0.05, 0.1, 0.5, 1 and 5	Only CF

3. RESULTS AND DISCUSSION

3.1 SURFACE FUNCTIONALIZATION MONITORING

FTIR spectroscopy was used to monitor each functionalization step employed to prepare the biorecognition layer onto the ZnO transducer, which conferred specificity for TC sensing. The results are displayed in Figure 4. As can be seen, the ZnO sample presents an intense absorption band at ~570 cm^{-1} due to Zn-O vibrations, which matches the position expected for the A_1(LO) vibrational mode of ZnO wurtzite [41]. Additionally, a broad band at approximately 3500 cm^{-1} and another at 1614 cm^{-1} are ascribed to OH stretching and OH bending vibrations [42], respectively. Other peaks at approximately 2970 and 900 cm^{-1} can also be identified in the ZnO bare sample and were attributed to vibrations related to the organic compounds present in the initial paste that were not completely degraded during the thermal treatment. After the surface modification of ZnO with APTES, the peaks assigned to OH groups vanished due to their condensation

reaction with APTES, forming new bonds, namely Si-O-Zn and Si-O stretching vibrations at 879 and 1014 cm^{-1} [42,43], respectively. Also, Si-O-Si stretching vibrations are identified at 1086 cm^{-1}, evidencing the existence of a silicate network layer on the ZnO surface [42]. In addition, the detection of the N-H bending vibrations at 1585 cm^{-1} confirms the presence of the primary amine from APTES [43]. After antibody covalent linkage, the peak assigned to the amine disappeared, as it is used to form the amide bond with the carboxylic group from the antibody. Furthermore, the typical amide A, amide I and amide II peaks at 3310, 1650 and 1540 cm^{-1}, respectively, arose from the presence of the antibody and are mainly due to the N-H stretching, C=O stretching and N-H plane bending together with C=N stretching vibrations, respectively, owing to the amide bonds of the protein backbone [44]. After the BSA passivation step, which is also a protein and that is physically adsorbed to the surface, the typical peaks of proteins were kept, as also observed in the antibody spectrum. Besides, the broader region between 3600 to 3200 cm^{-1} and the region between 1460 and 1330 cm^{-1} evidence the presence of hydrated BSA, corresponding to N-H stretching of free N-H groups, and COO^- stretching vibrations from hydrogen-bonded and free side groups [45]. We also note that the spectral changes observed in the Si-O vibration mode region after AB and BSA functionalization are due to some superimposition of vibrational modes from side chains of amino acids from these proteins [36,44].

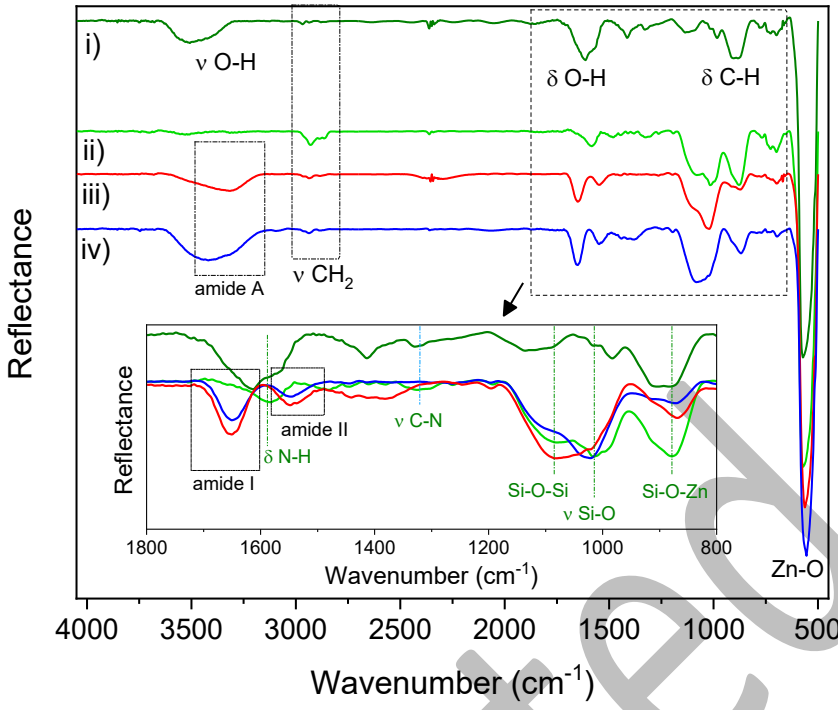

Figure 4. FTIR spectra of (i) ZnO, (ii) ZnO-APTES, (iii) antibody (AB) linked covalently to ZnO-APTES, and (iv) ZnO-APTES-AB with BSA as a passivation layer. The spectra were vertically shifted for clarity. Inset shows with higher detail the spectral region from 1800 to 800 cm^{-1}.

The functionalization process was further investigated by RT PL and PLE to infer the effect of each surface modification step in the luminescence features of the ZnO transducers. The results are depicted in Figure 5. As seen in Figure 5a, the PL spectra of the bare ZnO (pink line) is dominated by the NBE recombination in the UV spectral region peaked at 378 nm (~3.28 eV). This emission results from overlapping excitonic transitions, in particular the free exciton (FX) recombination, and has contributions from surface-related defect states that also appear in this spectral region [24,38,46]. Notwithstanding, the observed peak position is in line with the expected FX transition at RT [47–49], suggesting that this is the dominant recombination channel involved in the mentioned emission. This is further corroborated by the low-temperature PL data previously performed in similar ZnO samples [37,40]. In addition, the spectrum exhibits a

broad band in the visible spectral range, peaked in the green region (~510 nm/2.43 eV), which is a typical feature in the ZnO spectrum, either in the bulk or in nanocrystals [24,26,50,51]. This band has been associated with different types of defects, including intrinsic ones in the ZnO matrix, namely oxygen/zinc vacancies (V_O/V_{Zn}), Zn antisites (Zn_O), interstitial Zn atoms, transitions from Zn interstitials to Zn vacancies, or extrinsic impurities, as is the case of Cu ions [24,26,50,52,53]. In the case of structures with a high surface to volume ratio, such as the NTP investigated here, numerous works point towards the relationship between the unstructured green luminescence (GL) and defects present at the surface, as the surface properties tend to dominate over the bulk at the nanoscale. This is predominantly observed in structures produced by vapor-based methods [26,50,51,54], as is the case of the LAFD. Previous works from our group in ZnO NTP produced under similar conditions also suggest that the presence of surface defects in the crystals plays an important role in the observed GL [55]. Nevertheless, it should be stressed out that the GL often results from the overlapping of several radiative recombination channels emitting at the same spectral region, so despite in such ZnO nanostructures the contribution from the surface defects seems to have a dominant role [26,50,55], the presence of other emitting centers must be taken into account. Therefore, despite exhibiting similar peak positions and widths, the origin of the observed GL may be quite different from sample to sample, making it rather difficult to assess the nature of the specific defects involved. Regarding the PLE (Figure 5b), which was monitored at the maximum of the GL, an excitation peak is present at ~376 nm (~3.298 eV). This is related to absorption into near-bandgap electronic states, presenting a contribution from the thermally broadened FX resonance [56], and indicating that the optically active center(s) that contribute to the GL band is(are) preferentially populated by photons with energies equal or higher than the ZnO bandgap. Additionally, a tail of states extending towards longer

wavelengths, up to ~400 nm (~3.1 eV), is also visible. This tail of states is likely to arise from the asymmetries/inhomogeneities in the carrier's distribution between the states since ZnO possesses a high surface reactivity and a high density of defects and surface states [57], which can easily adsorb chemical species existent in its surroundings (e.g. O_2 or H_2O [58–62]), contributing to fluctuations in the charge density at the surface [63]. Indeed, the surrounding environment where the samples are stored and handed is an important source of acceptors/donors species at its surface, which are known to frequently contribute with additional charges to the surface [26,62,64,65], and have been linked to the appearance of broad visible bands in metal oxides as ZnO [50,62] or TiO_2 [66]. Moreover, the involvement of sub-bandgap states that can be induced by the mentioned surface-related defects should also play an important role in the population mechanisms of GL emission.

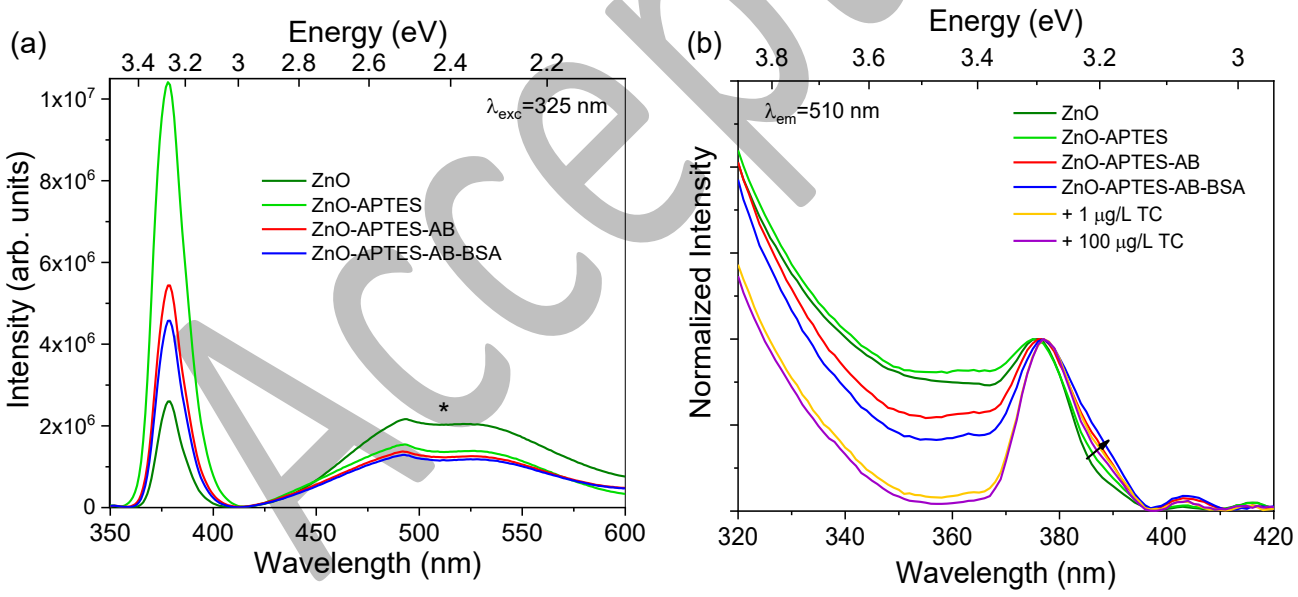

Figure 5. (a) RT PL spectra of the same ZnO transducer in each step of the functionalization process. The PL spectra were acquired under 325 nm excitation from a 450 W Xe lamp. The small depression in the region marked with an asterisk is an artefact produced by the measuring system. (b) RT normalized PLE spectra of the ZnO transducer in each step of the functionalization process, as well as for two different concentrations of TC. The spectra were obtained by monitoring at the maximum of the broad emission band (510 nm) and were normalized to the intensity of the peak at ca. 375-377 nm. The black arrow in the spectra highlights the increase in the tail of states with the surface modification.

After surface functionalization of the ZnO transducer with APTES (dark blue line in Figure 5a), a strong increase in the PL intensity was observed in the UV region (nearly 4× higher than the initial case), while the intensity of the GL slightly decreased. It is important to stress out that the optical alignment was kept during all the PL measurements depicted in Figure 5a, thus contributions from changes in the experimental configuration can be neglected in the observed signal increase. Such phenomenon is likely due to the (partial) passivation of surface defects present in the ZnO transducer, as previously discussed [37,40,46]. These defects, which can have different natures, can either contribute to the GL emission and/or act as non-radiative recombination channels, thus reducing the intensity of the overall PL emission. The presence of defects at the surface of the semiconductor is known to be responsible for charge accumulation at that region and the formation of a depletion region near the surface, causing the bending of the semiconductor electronic bands [26,67], as schematized in Figure 6a, which will be then ruled by the charge distribution at the surface. Hence, the built-in potential barrier at the surface induces a spatial separation of the carriers, which in turn reduces or even hinders the radiative recombination between photogenerated carriers in the bulk region, thereby strongly affecting the PL outcome. Therefore, the surface recombination processes are favored over the bulk transitions [26,66]. This is the case of the present bare ZnO sample, where the PL intensity of the GL (surface) is comparable to the NBE one (bulk). Therefore, when the ZnO nanostructures are capped with APTES (Figure 6b), it is proposed that the passivation of (part of) the surface defects takes place, which is expected to lead to a decrease in the surface charge, and, consequently, to the decrease of the energy band bending. In this way, a decrease of the depletion layer occurs, which, in turn, decreases the potential barrier that the carriers have to overcome from the bulk region to

radiatively recombine. Hence, part of the non-radiative defects are passivated and the contribution from the radiative defects at the surface is reduced (see the reduction of the GL intensity). This results in nearly all the crystal behaving as bulk, leading to an increase of the free carriers concentration, and thus to an enhancement of the excitonic PL intensity in the UV region. These observations are in line with the findings reported by Bera et al. [62], in which ZnO nanowires were capped with PVA. By capping the semiconductor nanostructures, the authors claim that the adsorption of species as O_2 on the surface becomes negligible and this resulted in a strong increase of both the photocurrent, as well as the intensity of the UV emission (at 379 nm), as the depletion layer at the surface is reduced. Similarly to the present case, the authors also observed an intensity decrease of the broad visible band, which in their case was seen to be present in the range 500-700 nm and was attributed to surface-adsorbed O_2 molecules [62]. Likewise, a similar phenomenon is likely occurring in the present ZnO nanotetrapods. By capping them with APTES, the presence of the adsorbed species at the surface that act as carrier traps and luminescence killers are reduced, leading to an increase in the PL intensity in the UV spectral region. The fact that the GL intensity only decreases slightly (~0.07× lower) in comparison to the strong increase (~4× higher) in the UV emission suggests a higher reduction of the non-radiative recombination centers in comparison to the surface states contributing to the GL. Concerning the PLE spectrum, barely any changes are perceived, indicating similar contributions from the density of states are involved in the recombinations recorded for the bare ZnO transducer. As the surface passivation does not have an impact on the energy separation of the valence and conduction bands, only on their bending, no significant changes are expected in the PLE spectrum, as observed experimentally.

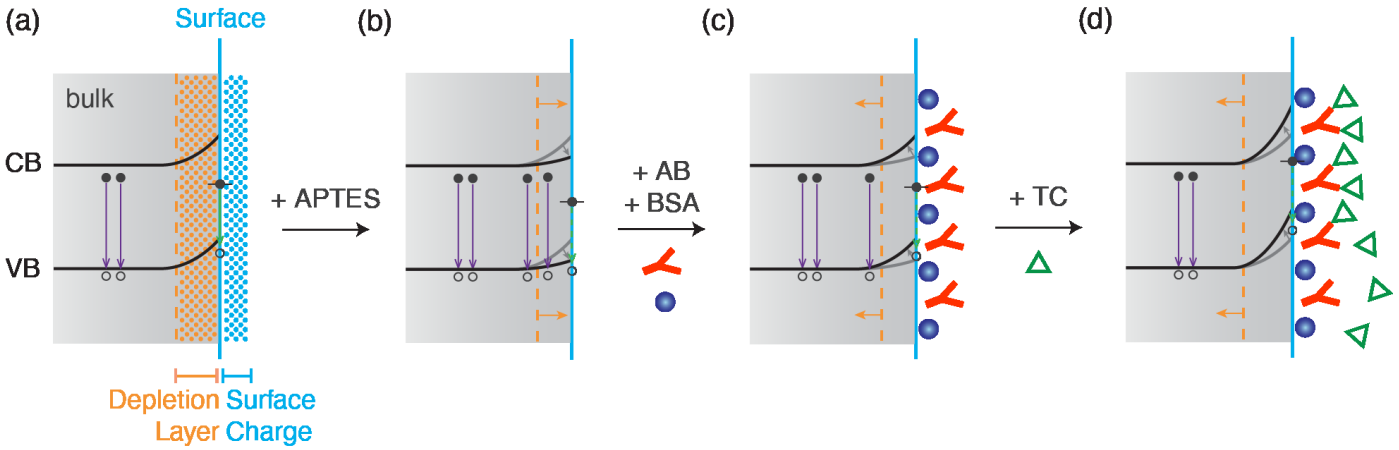

Figure 6. Schematic representation of the proposed band bending near the surface of ZnO during surface functionalization: (a) bare ZnO transducer, (b) after surface silanization with APTES, (c) after the immobilization of the AB and BSA proteins, and (d) upon incubation of the TC analyte. The dashed line in the green transition in figures (b) to (d) illustrates the decrease in its intensity compared with the situation (a). CB and VB stand for conduction and valence bands, respectively.

Upon AB and BSA immobilization, the PL spectra (light blue and green lines in Figure 5a, respectively) suffer a successive reduction in the intensity of the UV emission, while the GL remains barely unchanged. In the case of the PLE data (light blue and green lines in Figure 5b), a noticeable reduction in the intensity of the excitation spectra between 368 and 397 nm is observed, becoming more pronounced as the functionalization proceeds, and particularly after the incubation of the TC analyte on the sensor's surface (yellow and red lines in Figure 5b). Furthermore, a slight shift of the excitation band to longer wavelengths (lower energies) is also evident. For the bare ZnO transducer, this band is peaked at 376 nm (~3.298 eV), while after functionalization and TC incubation it appears at 377 nm (3.280 eV). Besides, an increase in the tail of states near the band edge onset absorption (at ~398 nm) is progressively observed after the addition of the AB, followed by BSA (see black arrow in Figure 5b). This evolution suggests an increase in the tail of states arising from higher charge fluctuations at the surface of the crystals due to the addition of the proteins (AB and BSA). Proteins are composed of amino acids that contain

side groups that can be neutral, positively or negatively charged and that together confer an overall charge to the protein [68,69]. The effective charge of the protein can be understood as the charge that is felt by other species in its proximity and dictates the force that is generated as a response to an electric field nearby, allowing it to participate in electrostatic interactions with other molecules and surfaces with opposite charge [25,68–70]. In an analogy with the heavily doped semiconductors [71], such additional and randomly distributed surface charge can be seen as electrostatic fluctuating potentials located at the surface of the semiconductor and compared to many-body interaction caused by a high density of impurities/defects in the lattice, which disrupts the periodic potential of the crystal, resulting in a broadening of the impurity levels and a considerable density of states tail extending into the bandgap of the semiconductor [72]. As well, an overlap with sub-bandgap electronic states related to surface defects already present in the samples cannot be disregarded for the population mechanisms involved in the recombination channels related to the GL (which is the one being monitored). Nevertheless, it is interesting to note that the PL intensity of the GL (Figure 5a) did not increase (slightly decrease instead) with AB and BSA addition, suggesting that if new surface states/defects are being created upon these functionalization steps, they do not contribute to this band and rather act as non-radiative recombination centers. Therefore, it is suggested that the charge density provided by the proteins when immobilized at the surface of the transducer, which are randomly distributed through the ZnO surface, will be responsible for the variation in the semiconductor's band bending. Upon the addition of the AB to the ZnO-APTES surface, the zero-length crosslinkers EDC promotes the formation of an amide bond between –COOH from AB and the $–NH_3^+$ from APTES [73], which will alter the charge distribution at the surface of the semiconductor. As this additional charge is placed on the ZnO surface, the bending of the electronic bands increases again, therefore promoting the

decrease in the excitonic-related emission seen in Figure 5. This situation is illustrated in Figure 6c, showing a new increase in the band bending when compared to the ZnO-APTES case. As so, the excitonic (bulk) contribution is reduced, explaining the decrease observed in the PL intensity in the NBE region. The difference in the GL is not so pronounced since most of its contributions are likely from surface related states that remained optically active after APTES surface modification. Due to the increase in the spatial separation of the carriers in such case, the radiative recombination between the energy bands of the semiconductor is partially hindered, while the contribution from the surface-related recombination processes remains [26], explaining the lesser effect observed in the GL intensity after the addition of the proteins. This phenomenon occurs upon AB immobilization and is further enhanced by adding the BSA to passivate the ZnO-APTES-AB surface. BSA has an effective charge of nearly -8.4 C at pH range from ~5.4 to 7 [68,74], which will also interact with the surface of the transducer by electrostatic, van der Waals forces and/or hydrogen bonds [73]. Thus, one can attribute the aforementioned PL intensity behavior to the interaction between ZnO-APTES surface and the immobilized proteins.

Finally, the strong decrease in the PLE intensity signal observed at wavelengths between ca. 350 and 367 nm when the TC analyte was added can also be explained by a new rearrangement of the global surface charge upon the specific interaction between the analyte and the biorecognition element. The formation of the immune complex can modify the balance of the charges of the AB that were contributing to the surface charge in ZnO and that now become involved in interactions with the antigen. Therefore, the interaction between the antibody and the transducer may be altered, inducing again changes in the charge at the transducer surface, which can lead to new alterations in its density of states, increasing even further the band bending (Figure 6d). The changes in the PLE spectra are also accompanied by an additional reduction of the PL intensity,

mainly in the UV spectral region, as seen in Figure 7a. In fact, this decrease is correlated with the increase in the TC concentration. As this concentration increased, a decrease in the overall intensity was verified. Even though a slight decrease was also observed for the GL, the effect was more pronounced in the NBE region (Figure 7a), in line with what was observed in previous works reporting the detection of other analytes [32,33,35,37]. As schematized in Figure 6d, a higher potential barrier is faced by the carriers when the analyte is introduced, increasing again the width of the depletion region, which leads to a higher region of the material where the radiative recombination is hindered. As so, the recombination can only occur in the inner regions of the crystals (bulk) and the PL intensity is quenched. In this case, this is mostly reflected in the FX recombination that dominates the PL spectra at RT. Consequently, this was the emission where we focused our attention on monitoring the PL intensity signal evolution depending on the TC concentration. Hence, it is proposed that the main phenomenon occurring upon analyte incubation is the bending of the electronic bands of the semiconductor, whose effect in the PL intensity can then be correlated with the analyte concentration, and thus used for sensing. This sensing mechanism is in line with the one suggested by Myndrul et al [36]. Even though in that case the authors observed an increase in the PL intensity of the broad visible band with increasing analyte concentration, the authors also suggested that such behavior was related to changes in the surface band bending caused by the adsorption of proteins, which could promote either the expansion (in the present case) or the constriction (in their case) of the depletion region, depending on the charge of the proteins bound to the surface. In their case, the antigen proteins were positively charged. Thus, as the ZnO is an n-type semiconductor, the presence of positively-charged species promoted a downward band bending and therefore a reduction of the surface potential. As the depletion region is reduced, more charged carriers are able to recombine at the bulk defect

states and thus the PL intensity increases [36]. However, in the present case, the TC molecules can have different protonation states depending on the pH where they are present, being considered a cation (TCH_3^+) for pH lower than 3.3, zwitterion (TCH_2^0) for pH values between 3.3 and 7.7 and an anion (TCH^- or TC^{2-}) for higher pH [75,76]. Therefore, at the pH used in the present experiments (pH=5.8), the TC molecules are expected to carry a neutral net charge, not participating in electrostatic interaction with the transducer. So, the present charge fluctuations will be mostly due to the AB, which has a lower isoelectric point than ZnO (~5.4 *vs.* 9.5) [77,78] and thus a negative net charge, inducing an upward band bending, as represented in Figure 6. As the TC is added, immune complexes are formed and a rearrangement of the charges happens at the surface of the semiconductor since some of the AB charges that were interacting with ZnO will now participate in interaction with the analyte, likely to live more negative charges at the semiconductor's surface promoting a further upward band bending and the decrease in the NBE intensity.

3.2 DETECTION OF TETRACYCLINE VIA PHOTOLUMINESCENCE

In line with the behavior described above, a progressive decrease in the NBE PL intensity with increasing concentration of TC incubated on the transducer surface was indeed verified in the present work for both concentration ranges tested (see Table 1). For the initial screening tests (sensors #1 to #4), TC solutions with concentrations in the range between 0.01 and 500 $\mu g\ L^{-1}$ were tested in order to understand the PL behavior in a broader range. Two regions of distinctive response were clearly identified, one in the range $0.01 - 1.0\ \mu g\ L^{-1}$ and another for $10 - 500\ \mu g\ L^{-1}$ (not shown). In the latter, the variation of the signal was less noticeable and a tendency of the sensing response to reach a plateau was observed, which may indicate that the majority of the antigen-binding sites

of anti-TC AB were already occupied at concentrations higher than 10 μg L^{-1}. Hence, no more antigen-AB complexes were able to form above this concentration. Nevertheless, taking into account that the range of TC concentrations usually found in freshwaters is much lower than this one (0.008 − 1 μg L^{-1} [2]), the range in which the sensor is less efficient is far from the one of interest. Therefore, as the range of interest corresponds to the former one, in which the response of the sensor appeared to be fairly linear when inspected in a semi-log scale, further sensing tests (sensors #5 to #13) were conducted for TC concentrations in the range between 0.001 and 5 μg L^{-1}. Figure 7a summarized the results and depicts the PL behavior of a representative sensor sample with increasing TC concentration (TC#10), where, as mentioned above, a clear decrease in the NBE recombination intensity is observed throughout the analyzed ranges. It is worth noting that this behavior was reproducible in all prepared sensors. Conversely, for the control sample (C#3, Figure 7b) corresponding to a sensor incubated only in the PS solution for consecutive times, barely any changes were identified in the PL intensity or spectral shape. Similar behaviors were also observed for ZnO-APTES-BSA samples (without anti-TC AB) incubated with the same TC concentrations as the sensors. Hence, these minor changes in the PL spectra (both shape and intensity) for the control samples clearly demonstrate that non-specific interactions between the transducer surface and the target analyte are negligible.

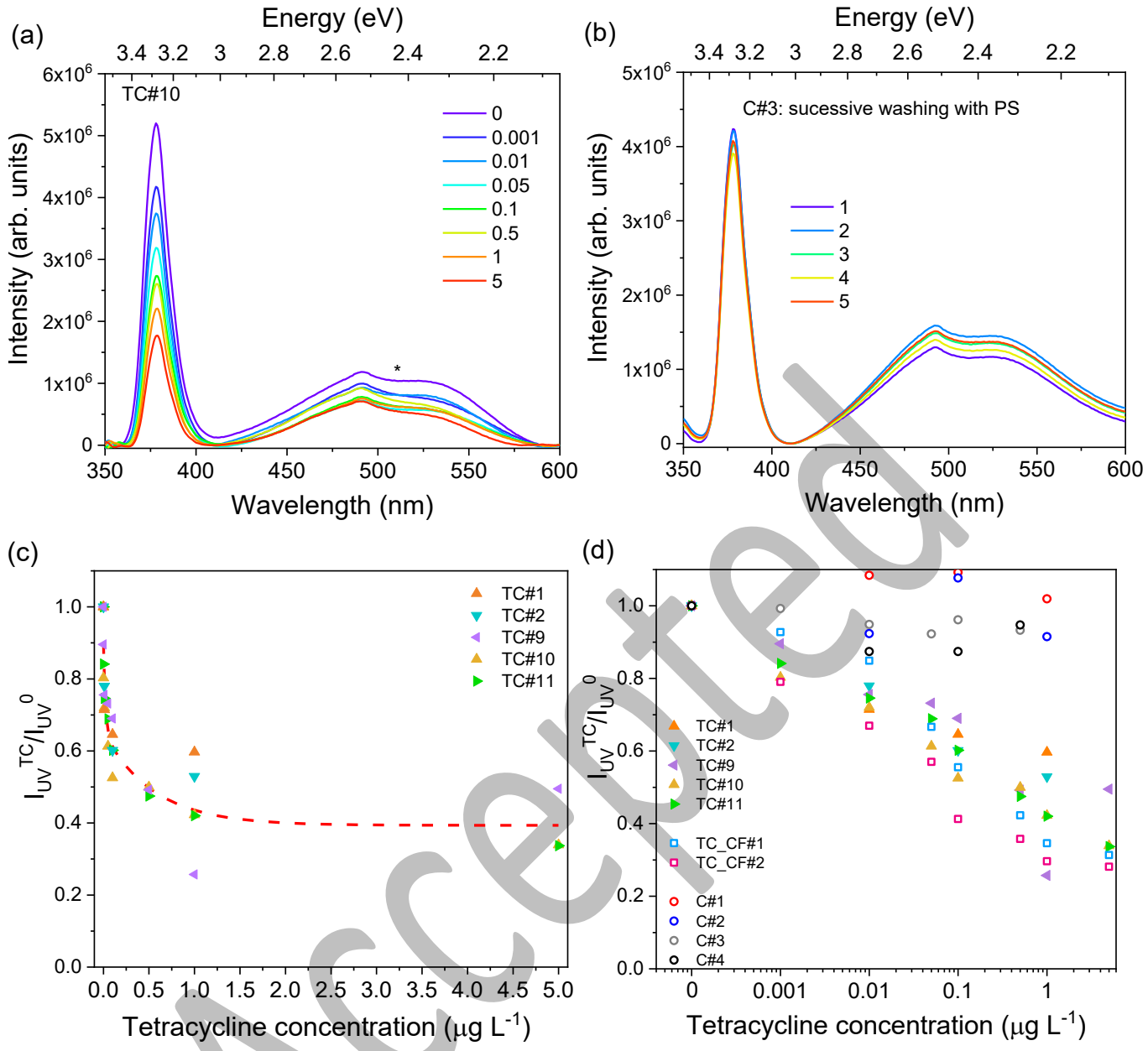

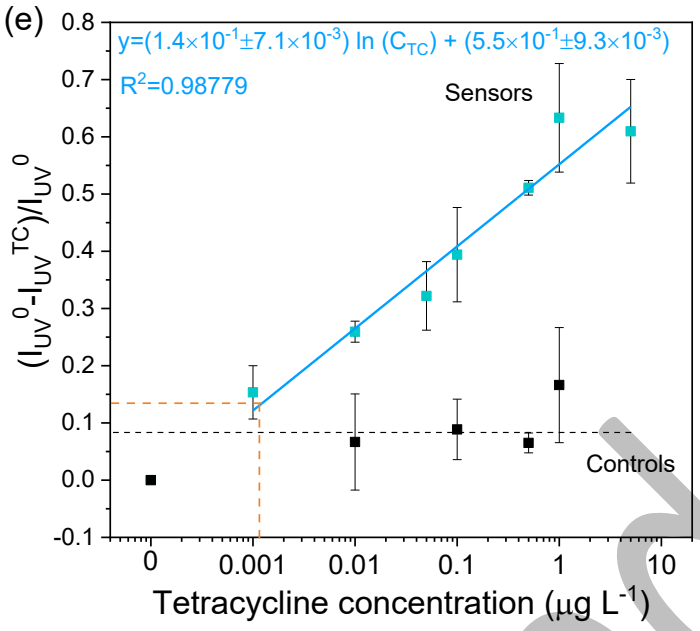

Figure 7. RT PL spectra acquired under 325 nm excitation for the ZnO-APTES-AB-BSA (a) as sensor incubated with different TC concentrations, and (b) as control incubated consecutive times with PS. (c) I_{UV}^{TC}/I_{UV}^{0} as a function of the TC concentration for representative sensors. The dashed red line was added as an aid to highlight the exponential decay of the intensity. (d) Semi-log representation of I_{UV}^{TC}/I_{UV}^{0} as a function of the TC concentration for representative sensors and control samples. The results obtained for the control sample incubated with PS (C#3) were also included for comparison, even though no TC was added in that case. (e) Average evolution of the sensing response $(I_{UV}^{0}-I_{UV}^{TC})/I_{UV}^{0}$ and the respective calibration curve for the present biosensors. The average evolution of the control samples was also added for comparison. The orange dashed lines denote the response value corresponding to 3σ (blank) used to calculate the LOD value, as described in the main text. In figures (d) and (e) the "0" value was added to the scale for representation purposes, corresponding to the intensity of the blank.

Figure 7c displays the I_{UV}^{TC}/I_{UV}^{0} ratio as a function of the TC concentration for selected sensor samples, demonstrating the exponential decay of the PL intensity for increasing TC concentrations. In Figure 7d, the same data is represented in a semi-log scale for selected sensors, together with the information for some control samples, as listed in Table 1. The semi-log scale was chosen to clearly depict the PL intensity decay in the lower concentration range, up to 1 μg L^{-1}. The data includes also additional control experiments performed with CF, which is an antibiotic also commonly found in

freshwaters all over the world at similar concentrations as TC (e.g., 0.309 μg L^{-1} in Portugal, 0.74 μg L^{-1} in Spain and 0.15 μg L^{-1} in the UK) [2]. Thus, it is important to evaluate the influence that its presence can have on the response of the sensors prepared for TC detection. As shown in Figure 7d, the control sample only incubated with CF (C#4) evidences a behavior similar to the previous controls, with only a slight variation in its PL intensity, which suggests that no reactions are occurring in such case, pointing to the specificity of the produced sensors for the target analyte. Additionally, the sensors incubated with the solutions having different TC concentrations and a fixed CF concentration (TC_CF#1,2) exhibit the same behavior as the one depicted for the sensors probed only in the presence of TC (open square in Figure 7d). Therefore, one can conclude that the presence of CF does not affect the sensing ability of the ZnO sensors in response to TC, thereby attesting to its reliability in more complex solutions.

When plotting the sensor's response (using Eq. 1) on a linear scale, a logarithmic increase is obtained, which can be then represented in a semi-log scale, as depicted in Figure 7e for the average sensors' response as a function of the TC concentration. In this way, a linear calibration curve can be defined. This type of response of the PL intensity of the analyte concentration was also observed in our previous work devoted to hCG detection [37]. Moreover, other works dedicated to TC detection also described calibration curves as a function of the concentration in a semi-log scale [20,79–81]. It is also worth mentioning that the values obtained for the response based on the PL intensity signal variation with increasing concentration of analyte are also in line with our previous experiments in luminescence-based immunosensors [37], as well as with results reported by other authors using ZnO nanostructures for the detection of different analytes [27,31,33,35,82]. Based on our experimental evidences, the present sensors exhibit a broad detection range between 0.001 and 1 μg L^{-1} that can be described by the calibration curve depicted in Figure 7e,

thus encompassing the typical concentration values found in freshwaters (0.008 and 1 μg L^{-1}) [2]. As can be seen in Figures 7c and 7e, the PL signal tends to stabilize for concentrations above 1 μg L^{-1}. Hence, as mentioned above for the wider range of TC concentrations tested, this suggests that above 1 μg L^{-1} the AB available to bind with the analyte became scarce and thus the immune complexes cannot be further formed, reaching the saturation limit of the present sensors. As no more changes at the surface charge distribution are taking place, the band bending remains stable and the PL intensity is kept approximately constant.

Another important figure of merit in sensor analysis is the LOD. In the case of a logarithmic dependence, this value can be estimated as the concentration corresponding to 3σ (blank) (see orange dashed lines in Figure 7e), in which σ (blank) is the standard deviation of the first control analyte concentration (0.001 μg L^{-1} in this case) [83–85]. In this way, a value of ~1.2 ng L^{-1} is estimated. Table 2 depicts a comparison of some recent results published in the literature for TC detection via luminescence-based biosensing relying on different transducer materials. As can be seen, even though the detection range reported here is narrower the some of the ones reported in the literature, the obtained LOD is one of the best values reported so far for TC quantification, not only in the luminescence-based biosensors listed in Table 2 but also when using other sensing approaches [13,17,86–91], attesting the cutting edge character of the here developed sensors.

Table 2. Summary of some representative results concerning TC detection using luminescence-based biosensors.

Transductor	Detection range	LOD	Ref.
Si quantum dots (QDs) & Cu^{2+}	11.32 – 1086.72 nM (~0.050 – 5 μg L^{-1})	0.92 nM (~4 ng L^{-1})	92
Carbon dots	0 – 100 μg L^{-1}	5 ng L^{-1}	87
$Tb(NO_3)_3 \cdot 6H_2O$ metal-organic framework	0 – 0.05 mM (~0 –222 μg L^{-1})	2.77 nM (~12 ng L^{-1})	88
Carbon dots	3 – 35 μM (~13 – 155 μg L^{-1})	12 nM (~53 ng L^{-1})	93
Pd nanoparticles & graphene QDs	40–90 μg L^{-1}& 100–500 μg L^{-1}	45 μg L^{-1}	89
N-acetyl-L-cysteine coated Ag nanoclusters	1.12 – 230 μM (~5 – 1021 μg L^{-1})	0.47 μM (~2 μg L^{-1})	91
Eu-functionalized ZnO QDs	0 – 3 μM (~0 – 13 μg L^{-1})	4 nM (~18 ng L^{-1})	94
ZnO NTP	0.001 – 1 μg L^{-1}	~1.2 ng L^{-1}	This work

As so, the present work demonstrates that the LAFD produced nanoscale ZnO-based sensors are suitable for PL intensity-based sensing, presenting reliable results for TC detection over a wide range of concentrations. Indeed, such an approach may contribute to the development of simple and portable solutions to assess the presence of this antibiotic in liquid alimentary product samples (e.g. milk) or water streams, for instance, which would have a beneficial impact in monitoring the undesirable and hidden antibiotic intake, both for humans as for aquatic species.

4. CONCLUSIONS

ZnO nanotetrapods were produced by the LAFD technique and deposited on FTO-coated glass substrates to be employed as transducers in biosensing devices for the detection of tetracycline. The antibiotic concentrations was assed via the monitoring of the ZnO luminescence intensity signal. To confer specificity to the envisaged sensors, the transducers were functionalized with anti-tetracycline antibodies via covalent binding using APTES as an intermediate agent that assure the proper antibody alignment to

maximize the analyte detection. FTIR analysis demonstrated that the proteins were successfully immobilized at the ZnO surface. The functionalization process was also monitored via PL and PLE, revealing that each surface modification step resulted in differences in the spectral response, mostly associated with band bending phenomena due to charge fluctuation at the semiconductor's surface, which, in turn, strongly affects the PL outcome. Due to the nanoscale dimensions of the produced ZnO structures, the surface phenomena rules over the bulk and small variations in the surface properties can be assessed. Thus, it was seen that the band bending increased with the surface charge upon analyte adsorption, leading to PL quenching, which was used as sensing mechanism for TC quantification. The PL signal, particularly the NBE recombination, quenched due to changes of the local electric field near the ZnO surface through the interaction of TC molecules with their specific antibodies, forming the immune complex. This quenching was seen to correlate with the TC concentration for a detection range between 0.001 and 1 μg L^{-1}, exhibiting an exponential decrease with increasing TC. A LOD of ~1.2 ng L^{-1} was estimated, which is amongst the lowest values reported up to date for state-of-the-art biosensors reported in the literature. Moreover, control experiments were performed either without the presence of the analyte or with a non-specific one, for which barely any changes were observed in the PL intensity spectra. Even when ciprofloxacin was added to the test solutions as interferent, the sensing response towards TC remained the same, attesting its specificity to the target analyte. Hence, the results reported here clearly demonstrate that reliable and high sensitive sensors for TC detection can be accomplished using the PL signal of the LAFD-produced ZnO nanostructures. Furthermore, this work corroborates that these ZnO-based transducers can provide a sensing platform that allows designing a biosensor for a target analyte by selecting the appropriate biorecognition

element, enabling the fabrication of sensing devices capable of probing relevant analytes with important clinical and environmental interest.

AUTHOR INFORMATION

Corresponding Author

*Joana Rodrigues: joana.catarina@ua.pt

Author Contributions

The manuscript was written through the contributions of all authors. All authors have given approval to the final version of the manuscript.

ACKNOWLEDGMENT

This work was developed within the scope of the project i3N, UIDB/50025/2020 & UIDP/50025/2020, financed by national funds through the FCT/MEC, as well as financially supported by FEDER funds through the COMPETE 2020 Programme and National Funds through FCT - Portuguese Foundation for Science and Technology under project PTDC/NAN-MAT/28755/2017 (POCI-01-0145-FEDER-028755). S. O. Pereira thanks i3N for her BPD grant BPD/UI96/5808/2017.

REFERENCES

(1) Phoon, B. L.; Ong, C. C.; Mohamed Saheed, M. S.; Show, P.-L.; Chang, J.-S.; Ling, T. C.; Lam, S. S.; Juan, J. C. Conventional and Emerging Technologies for Removal of Antibiotics from Wastewater. *J. Hazard. Mater.* **2020**, *400*, 122961. https://doi.org/10.1016/j.jhazmat.2020.122961.

(2) Danner, M. C.; Robertson, A.; Behrends, V.; Reiss, J. Antibiotic Pollution in Surface Fresh Waters: Occurrence and Effects. *Sci. Total Environ.* **2019**, *664*, 793–804. https://doi.org/10.1016/j.scitotenv.2019.01.406.

(3) World Health Organization. Antimicrobial Resistance: Global Report. **2014**. https://doi.org/10.1016/j.giec.2020.06.004.

(4) Sapadin, A. N.; Fleischmajer, R. Tetracyclines: Nonantibiotic Properties and Their Clinical Implications. *J. Am. Acad. Dermatol.* **2006**, *54* (2), 258–265. https://doi.org/10.1016/j.jaad.2005.10.004.

(5) Aga, D. S.; Goldfish, R.; Kulshrestha, P. Application of ELISA in Determining the Fate of Tetracyclines in Land-Applied Livestock Wastes. *Analyst* **2003**, *128*, 658–662. https://doi.org/10.1039/b301630g.

(6) Chen, Y.; Kong, D.; Liu, L.; Song, S.; Kuang, H.; Xu, C. Development of an ELISA and Immunochromatographic Assay for Tetracycline , Oxytetracycline , and Chlortetracycline Residues in Milk and Honey Based on the Class-Specific Monoclonal Antibody. *Food Anal. Methods* **2016**, *9*, 905–914. https://doi.org/10.1007/s12161-015-0262-z.

(7) Al-Afy, N.; Sereshti, H.; Hijazi, A.; Rashidi Nodeh, H. Determination of Three Tetracyclines in Bovine Milk Using Magnetic Solid Phase Extraction in Tandem with Dispersive Liquid-Liquid Microextraction Coupled with HPLC. *J. Chromatogr. B Anal. Technol. Biomed. Life Sci.* **2018**, *1092*, 480–488. https://doi.org/10.1016/j.jchromb.2018.06.049.

(8) Tu, C.; Dai, Y.; Xu, K.; Qi, M.; Wang, W.; Wu, L.; Wang, A. Determination of Tetracycline in Water and Honey by Iron (II , III)/ Aptamer-Based Magnetic Solid- Phase Extraction with High-Performance Liquid Chromatography Analysis. *Anal. Lett.* **2019**, *52*, 1653–1669.

https://doi.org/10.1080/00032719.2018.1560458.

(9) Pollap, A.; Kochana, J. Electrochemical Immunosensors for Antibiotic Detection. *Biosensors* **2019**, *9* (2), 61. https://doi.org/10.3390/bios9020061.

(10) Du, F.; Sun, L.; Tan, W.; Wei, Z.; Nie, H.; Huang, Z.; Ruan, G.; Li, J. Magnetic Stir Cake Sorptive Extraction of Trace Tetracycline Antibiotics in Food Samples: Preparation of Metal–Organic Framework-Embedded PolyHIPE Monolithic Composites, Validation and Application. *Anal. Bioanal. Chem.* **2019**, *411* (10), 2239–2248. https://doi.org/10.1007/s00216-019-01660-1.

(11) Zhou, L.; Li, D. J.; Gai, L.; Wang, J. P.; Li, Y. Bin. Electrochemical Aptasensor for the Detection of Tetracycline with Multi-Walled Carbon Nanotubes Amplification. *Sensors Actuators, B Chem.* **2012**, *162* (1), 201–208. https://doi.org/10.1016/j.snb.2011.12.067.

(12) Kim, Y. J.; Kim, Y. S.; Niazi, J. H.; Gu, M. B. Electrochemical Aptasensor for Tetracycline Detection. *Bioprocess Biosyst. Eng.* **2010**, *33* (1), 31–37. https://doi.org/10.1007/s00449-009-0371-4.

(13) Jalalian, S. H.; Karimabadi, N.; Ramezani, M.; Abnous, K.; Taghdisi, S. M. Electrochemical and Optical Aptamer-Based Sensors for Detection of Tetracyclines. *Trends Food Sci. Technol.* **2018**, *73*, 45–57. https://doi.org/10.1016/j.tifs.2018.01.009.

(14) Zhang, L.; Chen, L. Fluorescence Probe Based on Hybrid Mesoporous Silica/Quantum Dot/Molecularly Imprinted Polymer for Detection of Tetracycline. *ACS Appl. Mater. Interfaces* **2016**, *8* (25), 16248–16256. https://doi.org/10.1021/acsami.6b04381.

(15) Ouyang, Q.; Liu, Y.; Chen, Q.; Guo, Z.; Zhao, J.; Li, H.; Hu, W. Rapid and Specific Sensing of Tetracycline in Food Using a Novel Upconversion

Aptasensor. *Food Control* **2017**, *81*, 156–163. https://doi.org/10.1016/j.foodcont.2017.06.004.

(16) Wang, S.; Dong, Y.; Liang, X. Development of a SPR Aptasensor Containing Oriented Aptamer for Direct Capture and Detection of Tetracycline in Multiple Honey Samples. *Biosens. Bioelectron.* **2018**, *109*, 1–7. https://doi.org/10.1016/j.bios.2018.02.051.

(17) Gao, W.; Li, P.; Qin, S.; Huang, Z.; Cao, Y.; Liu, X. A Highly Sensitive Tetracycline Sensor Based on a Combination of Magnetic Molecularly Imprinted Polymer Nanoparticles and Surface Plasmon Resonance Detection. *Microchim. Acta* **2019**, *186*, 637. https://doi.org/10.1007/s00604-019-3718-9.

(18) Pinheiro, P. C.; Fateixa, S.; Nogueira, H. I. S.; Trindade, T. Magnetite-Supported Gold Nanostars for the Uptake and SERS Detection of Tetracycline. *Nanomaterials* **2019**, *9* (1). https://doi.org/10.3390/nano9010031.

(19) Pagano, R.; Ottolini, M.; Valli, L.; Bettini, S.; Giancane, G. Ag Nanodisks Decorated Filter Paper as a SERS Platform for Nanomolar Tetracycline Detection. *Colloids Surfaces A Physicochem. Eng. Asp.* **2021**, *624*, 126787. https://doi.org/10.1016/j.colsurfa.2021.126787.

(20) Qian, J.; Xing, C.; Ge, Y.; Li, R.; Li, A.; Yan, W. Gold Nanostars-Enhanced Raman Fingerprint Strip for Rapid Detection of Trace Tetracycline in Water Samples. *Spectrochim. Acta Part A Mol. Biomol. Spectrosc.* **2020**, *232*, 118146. https://doi.org/10.1016/j.saa.2020.118146.

(21) Li, H.; Chen, Q.; Mehedi Hassan, M.; Chen, X.; Ouyang, Q.; Guo, Z.; Zhao, J. A Magnetite/PMAA Nanospheres-Targeting SERS Aptasensor for Tetracycline Sensing Using Mercapto Molecules Embedded Core/Shell Nanoparticles for Signal Amplification. *Biosens. Bioelectron.* **2017**, *92*, 192–199.

https://doi.org/10.1016/j.bios.2017.02.009.

(22) Sarangi, S. N.; Nozaki, S.; Sahu, S. N. ZnO Nanorod-Based Non-Enzymatic Optical Glucose Biosensor. *J. Biomed. Nanotechnol.* **2015**, *11* (6), 988–996. https://doi.org/10.1166/jbn.2015.2048.

(23) Kumar, S.; Ahlawat, W.; Kumar, R.; Dilbaghi, N. Graphene, Carbon Nanotubes, Zinc Oxide and Gold as Elite Nanomaterials for Fabrication of Biosensors for Healthcare. *Biosens. Bioelectron.* **2015**, *70*, 498–503. https://doi.org/10.1016/j.bios.2015.03.062.

(24) Özgür, U.; Alivov, Y. I.; Liu, C.; Teke, A.; Reshchikov, M. A.; Doğan, S.; Avrutin, V.; Cho, S.-J.; Morkoç, H. A Comprehensive Review of ZnO Materials and Devices. *J. Appl. Phys.* **2005**, *98* (4), 041301. https://doi.org/10.1063/1.1992666.

(25) Tereshchenko, A.; Bechelany, M.; Viter, R.; Khranovskyy, V.; Smyntyna, V.; Starodub, N.; Yakimova, R. Optical Biosensors Based on ZnO Nanostructures: Advantages and Perspectives. A Review. *Sensors and Actuators, B: Chemical*. June 2016, pp 664–677. https://doi.org/10.1016/j.snb.2016.01.099.

(26) Rodrigues, J.; Ben Sedrine, N.; Correia, M. R.; Monteiro, T. Photoluminescence Investigations of ZnO Micro/Nanostructures. *Mater. Today Chem.* **2020**, *16*, 100243. https://doi.org/10.1016/j.mtchem.2020.100243.

(27) Sodzel, D.; Khranovskyy, V.; Beni, V.; Turner, A. P. F.; Viter, R.; Eriksson, M. O.; Holtz, P.-O.; Janot, J.-M.; Bechelany, M.; Balme, S.; et al. Continuous Sensing of Hydrogen Peroxide and Glucose via Quenching of the UV and Visible Luminescence of ZnO Nanoparticles. *Microchim. Acta* **2015**, *182* (9–10), 1819–1826. https://doi.org/10.1007/s00604-015-1493-9.

(28) Hariharan, S.; Karthikeyan, B. Band Bending Effect Induced Non-Enzymatic

Highly Sensitive Glucose Sensing in ZnO Nanoparticles. *J. Lumin.* **2017**, *183*, 1–6. https://doi.org/10.1016/j.jlumin.2016.10.046.

(29) Briones, M.; Busó-Rogero, C.; Catalán-Gómez, S.; García-Mendiola, T.; Pariente, F.; Redondo-Cubero, A.; Lorenzo, M. E. ZnO Nanowire-Based Fluorometric Enzymatic Assays for Lactate and Cholesterol. *Microchim. Acta* **2020**, *187* (3), 180. https://doi.org/10.1007/s00604-020-4137-7.

(30) Viter, R.; Khranovskyy, V.; Starodub, N.; Ogorodniichuk, Y.; Gevelyuk, S.; Gertnere, Z.; Poletaev, N.; Yakimova, R.; Erts, D.; Smyntyna, V.; et al. Application of Room Temperature Photoluminescence From ZnO Nanorods for Salmonella Detection. *IEEE Sens. J.* **2014**, *14* (6), 2028–2034. https://doi.org/10.1109/JSEN.2014.2309277.

(31) Tereshchenko, A.; Fedorenko, V.; Smyntyna, V.; Konup, I.; Konup, A.; Eriksson, M.; Yakimova, R.; Ramanavicius, A.; Balme, S.; Bechelany, M. ZnO Films Formed by Atomic Layer Deposition as an Optical Biosensor Platform for the Detection of Grapevine Virus A-Type Proteins. *Biosens. Bioelectron.* **2017**, *92*, 763–769. https://doi.org/10.1016/j.bios.2016.09.071.

(32) Viter, R.; Savchuk, M.; Starodub, N.; Balevicius, Z.; Tumenas, S.; Ramanaviciene, A.; Jevdokimovs, D.; Erts, D.; Iatsunskyi, I.; Ramanavicius, A. Photoluminescence Immunosensor Based on Bovine Leukemia Virus Proteins Immobilized on the ZnO Nanorods. *Sensors Actuators B Chem.* **2019**, *285*, 601–606. https://doi.org/10.1016/j.snb.2019.01.054.

(33) Tamashevski, A.; Harmaza, Y.; Viter, R.; Jevdokimovs, D.; Poplausks, R.; Slobozhanina, E.; Mikoliunaite, L.; Erts, D.; Ramanaviciene, A.; Ramanavicius, A. Zinc Oxide Nanorod Based Immunosensing Platform for the Determination of Human Leukemic Cells. *Talanta* **2019**, *200*, 378–386.

https://doi.org/10.1016/j.talanta.2019.03.064.

(34) Tamashevski, A.; Harmaza, Y.; Slobozhanina, E.; Viter, R.; Iatsunskyi, I. Photoluminescent Detection of Human T-Lymphoblastic Cells by ZnO Nanorods. *Molecules* **2020**, *25* (14), 3168. https://doi.org/10.3390/molecules25143168.

(35) Viter, R.; Savchuk, M.; Iatsunskyi, I.; Pietralik, Z.; Starodub, N.; Shpyrka, N.; Ramanaviciene, A.; Ramanavicius, A. Analytical, Thermodynamical and Kinetic Characteristics of Photoluminescence Immunosensor for the Determination of Ochratoxin A. *Biosens. Bioelectron.* **2018**, *99*, 237–243. https://doi.org/10.1016/j.bios.2017.07.056.

(36) Myndrul, V.; Coy, E.; Bechelany, M.; Iatsunskyi, I. Photoluminescence Label-Free Immunosensor for the Detection of Aflatoxin B1 Using Polyacrylonitrile/Zinc Oxide Nanofibers. *Mater. Sci. Eng. C* **2021**, *118*, 111401. https://doi.org/10.1016/j.msec.2020.111401.

(37) Rodrigues, J.; Pereira, S. O.; Santos, N. F.; Rodrigues, C.; Costa, F. M.; Monteiro, T. Insights on Luminescence Quenching of ZnO Tetrapods in the Detection of HCG. *Appl. Surf. Sci.* **2020**, *527*, 146813. https://doi.org/10.1016/j.apsusc.2020.146813.

(38) Rodrigues, J.; Fernandes, A. J. S.; Monteiro, T.; Costa, F. M. A Review on the Laser-Assisted Flow Deposition Method: Growth of ZnO Micro and Nanostructures. *CrystEngComm* **2019**, *21* (7), 1071–1090. https://doi.org/10.1039/c8ce01773e.

(39) Rodrigues, J.; Cerqueira, A. F. R.; Sousa, M. G.; Santos, N. F.; Pimentel, A.; Fortunato, E.; da Cunha, A. F.; Monteiro, T.; Costa, F. M. Exploring the Potential of Laser Assisted Flow Deposition Grown ZnO for Photovoltaic Applications.

Mater. Chem. Phys. **2016**, *177*, 322–329. https://doi.org/10.1016/j.matchemphys.2016.04.033.

(40) Zanoni, J.; Moura, J. P.; Santos, N. F.; Carvalho, A. F.; Fernandes, A. J. S.; Monteiro, T.; Costa, F. M.; Pereira, S. O.; Rodrigues, J. Dual Transduction of H2O2 Detection Using ZnO/Laser-Induced Graphene Composites. *Chemosensors* **2021**, *9*, 102.

(41) Cuscó, R.; Alarcón-Lladó, E.; Ibáñez, J.; Artús, L.; Jiménez, J.; Wang, B.; Callahan, M. Temperature Dependence of Raman Scattering in ZnO. *Phys. Rev. B* **2007**, *75* (16), 165202. https://doi.org/10.1103/PhysRevB.75.165202.

(42) Hao, L.; Hu, Y.; Zhang, Y.; Wei, W.; Hou, X.; Guo, Y.; Hu, X.; Jiang, D. Enhancing the Mechanical Performance of Poly(Ether Ether Ketone)/Zinc Oxide Nanocomposites to Provide Promising Biomaterials for Trauma and Orthopedic Implants. *RSC Adv.* **2018**, *8* (48), 27304–27317. https://doi.org/10.1039/C8RA01736K.

(43) Jaramillo, A. F.; Baezruza, R.; Montoya, L. F.; Medinam, C.; Pérez-Tijerina, E.; Salazar, F.; Rojas, D.; Melendrez, M. F. Estimation of the Surface Interaction Mechanism of ZnO Nanoparticles Modified with Organosilane Groups by Raman Spectroscopy. *Ceram. Int.* **2017**, *43* (15), 11838–11847.

(44) Barth, A. Infrared Spectroscopy of Proteins. *Biochim. Biophys. Acta - Bioenerg.* **2007**, *1767* (9), 1073–1101. https://doi.org/10.1016/j.bbabio.2007.06.004.

(45) Grdadolnik, J.; Maréchal, Y. Bovine Serum Albumin Observed by Infrared Spectrometry. I. Methodology, Structural Investigation, and Water Uptake. *Biopolymers* **2001**, *62* (1), 40–53. https://doi.org/10.1002/1097-0282(2001)62:1<40::AID-BIP60>3.0.CO;2-C.

(46) Rodrigues, J.; Holz, T.; Fath Allah, R.; Gonzalez, D.; Ben, T.; Correira, M. R.;

Monteiro, T.; Costa, F. M. Effect of the N2 and H2 Plasma Treatments on Band Edge Emission of ZnO Microrods. *Sci. Rep.* **2015**, *5*, 10783. https://doi.org/10.1038/srep10783.

(47) Wang, L.; Giles, N. C. Temperature Dependence of the Free-Exciton Transition Energy in Zinc Oxide by Photoluminescence Excitation Spectroscopy. *J. Appl. Phys.* **2003**, *94* (2), 973. https://doi.org/10.1063/1.1586977.

(48) Bagnall, D. M.; Chen, Y. F.; Shen, M. Y.; Zhu, Z.; Goto, T.; Yao, T. Room Temperature Excitonic Stimulated Emission from Zinc Oxide Epilayers Grown by Plasma-Assisted MBE. *J. Cryst. Growth* **1998**, *184–185*, 605–609. https://doi.org/10.1016/S0022-0248(98)80127-9.

(49) Klingshirn, C. F.; Waag, A.; Hoffmann, A.; Geurts, J. *Zinc Oxide: From Fundamental Properties Towards Novel Applications*, 1st ed.; Springer, 2010.

(50) Djurišić, A. B.; Leung, Y. H.; Tam, K. H.; Hsu, Y. F.; Ding, L.; Ge, W. K.; Zhong, Y. C.; Wong, K. S.; Chan, W. K.; Tam, H. L.; et al. Defect Emissions in ZnO Nanostructures. *Nanotechnology* **2007**, *18* (9), 095702. https://doi.org/10.1088/0957-4484/18/9/095702.

(51) Djurišić, A. B.; Leung, Y. H.; Tam, K. H.; Ding, L.; Ge, W. K.; Chen, H. Y.; Gwo, S. Green, Yellow, and Orange Defect Emission from ZnO Nanostructures: Influence of Excitation Wavelength. *Appl. Phys. Lett.* **2006**, *88* (10), 103107. https://doi.org/10.1063/1.2182096.

(52) Jagadish, C.; Pearton, S. *Zinc Oxide Bulk, Thin Films and Nanostructures*; Elsevier, 2006. https://doi.org/10.1016/B978-0-08-044722-3.X5000-3.

(53) Dingle, R. Luminescent Transitions Associated With Divalent Copper Impurities and the Green Emission from Semiconducting Zinc Oxide. *Phys. Rev. Lett.* **1969**, *23* (11), 579–581. https://doi.org/10.1103/PhysRevLett.23.579.

(54) Li, D.; Leung, Y. H.; Djurišić, A. B.; Liu, Z. T.; Xie, M. H.; Shi, S. L.; Xu, S. J.; Chan, W. K. Different Origins of Visible Luminescence in ZnO Nanostructures Fabricated by the Chemical and Evaporation Methods. *Appl. Phys. Lett.* **2004**, *85* (9), 1601–1603. https://doi.org/10.1063/1.1786375.

(55) Rodrigues, J.; Pimentel, A.; Fortunato, E.; Monteiro, T.; Costa, F. M. Photocatalytic Activity of Laser-Processed ZnO Micro/Nanocrystals. *Phys. status solidi* **2018**, *215* (19), 1800155. https://doi.org/10.1002/pssa.201800155.

(56) Postica, V.; Gröttrup, J.; Adelung, R.; Lupan, O.; Mishra, A. K.; de Leeuw, N. H.; Ababii, N.; Carreira, J. F. C.; Rodrigues, J.; Sedrine, N. Ben; et al. Multifunctional Materials: A Case Study of the Effects of Metal Doping on ZnO Tetrapods with Bismuth and Tin Oxides. *Adv. Funct. Mater.* **2017**, *27* (6), 1604676. https://doi.org/10.1002/adfm.201604676.

(57) Djurišić, A. B.; Liu, X.; Leung, Y. H. Zinc Oxide Films and Nanomaterials for Photovoltaic Applications. *Phys. status solidi - Rapid Res. Lett.* **2014**, *8* (2), 123–132. https://doi.org/10.1002/pssr.201300103.

(58) Wöll, C. The Chemistry and Physics of Zinc Oxide Surfaces. *Prog. Surf. Sci.* **2007**, *82* (2–3), 55–120. https://doi.org/10.1016/j.progsurf.2006.12.002.

(59) Dulub, O.; Diebold, U.; Kresse, G. Novel Stabilization Mechanism on Polar Surfaces: ZnO(0001)-Zn. *Phys. Rev. Lett.* **2003**, *90* (1), 016102. https://doi.org/10.1103/PhysRevLett.90.016102.

(60) Meyer, B. First-Principles Study of the Polar O-Terminated ZnO Surface in Thermodynamic Equilibrium with Oxygen and Hydrogen. *Phys. Rev. B* **2004**, *69* (4), 045416. https://doi.org/10.1103/PhysRevB.69.045416.

(61) Urgessa, Z. N.; Botha, J. R.; Eriksson, M. O.; Mbulanga, C. M.; Dobson, S. R.; Tankio Djiokap, S. R.; Karlsson, K. F.; Khranovskyy, V.; Yakimova, R.; Holtz,

P.-O. Low Temperature near Band Edge Recombination Dynamics in ZnO Nanorods. *J. Appl. Phys.* **2014**, *116* (12), 123506. https://doi.org/10.1063/1.4896488.

(62) Bera, A.; Basak, D. Effect of Surface Capping with Poly(Vinyl Alcohol) on the Photocarrier Relaxation of ZnO Nanowires. *ACS Appl. Mater. Interfaces* **2009**, *1* (9), 2066–2070. https://doi.org/10.1021/am900422y.

(63) Zhou, X.; Kuang, Q.; Jiang, Z.-Y.; Xie, Z.-X.; Xu, T.; Huang, R.-B.; Zheng, L.-S. The Origin of Green Emission of ZnO Microcrystallites: Surface-Dependent Light Emission Studied by Cathodoluminescence. *J. Phys. Chem. C* **2007**, *111* (32), 12091–12093. https://doi.org/10.1021/jp071928h.

(64) Fan, Z.; Wang, D.; Chang, P.-C.; Tseng, W.-Y.; Lu, J. G. ZnO Nanowire Field-Effect Transistor and Oxygen Sensing Property. *Appl. Phys. Lett.* **2004**, *85*, 5923. https://doi.org/https://doi.org/10.1063/1.1836870.

(65) Chakrapani, V.; Pendyala, C.; Kash, K.; Anderson, A. B.; Sunkara, M. K.; Angus, J. C. Electrochemical Pinning of the Fermi Level: Mediation of Photoluminescence from Gallium Nitride and Zinc Oxide. *J. Am. Chem. Soc.* **2008**, *130* (39), 12944–12952. https://doi.org/10.1021/ja710999r.

(66) Mondal, S.; Basak, D. Defect Controlled Tuning of the Ratio of Ultraviolet to Visible Light Emission in TiO2 Thin Films. *J. Lumin.* **2016**, *179*, 480–486. https://doi.org/10.1016/j.jlumin.2016.07.046.

(67) Liao, Z.-M.; Zhang, H.-Z.; Zhou, Y.-B.; Xu, J.; Zhang, J.-M.; Yu, D.-P. Surface Effects on Photoluminescence of Single ZnO Nanowires. *Phys. Lett. A* **2008**, *372* (24), 4505–4509. https://doi.org/10.1016/j.physleta.2008.04.013.

(68) Böhme, U.; Scheler, U. Effective Charge of Bovine Serum Albumin Determined by Electrophoresis NMR. *Chem. Phys. Lett.* **2007**, *435* (4–6), 342–345.

https://doi.org/10.1016/j.cplett.2006.12.068.

(69) Gitlin, I.; Carbeck, J. D.; Whitesides, G. M. Why Are Proteins Charged? Networks of Charge–Charge Interactions in Proteins Measured by Charge Ladders and Capillary Electrophoresis. *Angew. Chemie Int. Ed.* **2006**, *45* (19), 3022–3060. https://doi.org/10.1002/anie.200502530.

(70) Nelson, D. L.; Cox, M. M. *Lehninger Principles of Biochemistry, Third Edition*, 3rd ed.; Worth Publishtrs Inc.,: New York, 2000.

(71) Levanyuk, A. P.; Osipov, V. V. Edge Luminescence of Direct-Gap Semiconductors. *Sov. Phys. Uspekhi* **1981**, *24* (3), 187–215. https://doi.org/10.1070/PU1981v024n03ABEH004770.

(72) Falcão, B. P.; Leitão, J. P.; Ricardo, L.; Águas, H.; Martins, R.; Pereira, R. N. Recombination of Photo-Generated Charge Carriers in H-Terminated and (Photo-)Oxidized Silicon Nanoparticles. *Appl. Mater. Today* **2021**, *23*, 101071. https://doi.org/10.1016/j.apmt.2021.101071.

(73) Vashist, S. K.; Lam, E.; Hrapovic, S.; Male, K. B.; Luong, J. H. T. Immobilization of Antibodies and Enzymes on 3-Aminopropyltriethoxysilane-Functionalized Bioanalytical Platforms for Biosensors and Diagnostics. *Chem. Rev.* **2014**, *114* (21), 11083–11130. https://doi.org/10.1021/cr5000943.

(74) Barbosa, L. R. S.; Ortore, M. G.; Spinozzi, F.; Mariani, P.; Bernstorff, S.; Itri, R. The Importance of Protein-Protein Interactions on the PH-Induced Conformational Changes of Bovine Serum Albumin: A Small-Angle X-Ray Scattering Study. *Biophys. J.* **2010**, *98* (1), 147–157. https://doi.org/10.1016/j.bpj.2009.09.056.

(75) Yu, F.; Ma, J.; Han, S. Adsorption of Tetracycline from Aqueous Solutions onto Multi-Walled Carbon Nanotubes with Different Oxygen Contents. *Sci. Rep.*

2015, *4* (1), 5326. https://doi.org/10.1038/srep05326.

(76) Kulshrestha, P.; Giese, R. F.; Aga, D. S. Investigating the Molecular Interactions of Oxytetracycline in Clay and Organic Matter: Insights on Factors Affecting Its Mobility in Soil. *Environ. Sci. Technol.* **2004**, *38* (15), 4097–4105. https://doi.org/10.1021/es034856q.

(77) Horká, M.; Vykydalová, M.; Růžička, F.; Šalplachta, J.; Holá, V.; Dvořáčková, M.; Kubesová, A.; Šlais, K. CIEF Separation, UV Detection, and Quantification of Ampholytic Antibiotics and Bacteria from Different Matrices. *Anal. Bioanal. Chem.* **2014**, *406* (25), 6285–6296. https://doi.org/10.1007/s00216-014-8053-8.

(78) Ahmad, M.; Pan, C.; Gan, L.; Nawaz, Z.; Zhu, J. Highly Sensitive Amperometric Cholesterol Biosensor Based on Pt-Incorporated Fullerene-like ZnO Nanospheres. *J. Phys. Chem. C* **2010**, *114* (1), 243–250. https://doi.org/10.1021/jp9089497.

(79) Rouhbakhsh, Z.; Verdian, A.; Rajabzadeh, G. Design of a Liquid Crystal-Based Aptasensing Platform for Ultrasensitive Detection of Tetracycline. *Talanta* **2020**, *206*, 120246. https://doi.org/10.1016/j.talanta.2019.120246.

(80) Chen, J.; Chen, S.; Li, F. Instrument-Free Visual Detection of Tetracycline on an Autocatalytic DNA Machine Using a Caged G-Quadruplex as the Signal Reporter. *Chem. Commun.* **2017**, *53* (62), 8743–8746. https://doi.org/10.1039/C7CC04083K.

(81) Han, Q.; Wang, R.; Xing, B.; Chi, H.; Wu, D.; Wei, Q. Label-Free Photoelectrochemical Aptasensor for Tetracycline Detection Based on Cerium Doped CdS Sensitized BiYWO6. *Biosens. Bioelectron.* **2018**, *106*, 7–13. https://doi.org/10.1016/j.bios.2018.01.051.

(82) Viter, R.; Tereshchenko, A.; Smyntyna, V.; Ogorodniichuk, J.; Starodub, N.;

Yakimova, R.; Khranovskyy, V.; Ramanavicius, A. Toward Development of Optical Biosensors Based on Photoluminescence of TiO2 Nanoparticles for the Detection of Salmonella. *Sensors Actuators B Chem.* **2017**, *252*, 95–102. https://doi.org/10.1016/j.snb.2017.05.139.

(83) Leitão, C.; Leal-Junior, A.; Almeida, A. R.; Pereira, S. O.; Costa, F. M.; Pinto, J. L.; Marques, C. Cortisol AuPd Plasmonic Unclad POF Biosensor. *Biotechnol. Reports* **2021**, *29*, e00587. https://doi.org/10.1016/j.btre.2021.e00587.

(84) Gauglitz, G. Analytical Evaluation of Sensor Measurements. *Anal. Bioanal. Chem.* **2018**, *410* (1), 5–13. https://doi.org/10.1007/s00216-017-0624-z.

(85) Sevenler, D.; Trueb, J.; Ünlü, M. S. Beating the Reaction Limits of Biosensor Sensitivity with Dynamic Tracking of Single Binding Events. *Proc. Natl. Acad. Sci.* **2019**, *116* (10), 4129–4134. https://doi.org/10.1073/pnas.1815329116.

(86) Besharati, M.; Tabrizi, M. A.; Molaabasi, F.; Saber, R.; Shamsipur, M.; Hamedi, J.; Hosseinkhani, S. Novel Enzyme-based Electrochemical and Colorimetric Biosensors for Tetracycline Monitoring in Milk. *Biotechnol. Appl. Biochem.* **2021**, bab.2078. https://doi.org/10.1002/bab.2078.

(87) Guo, F.; Zhu, Z.; Zheng, Z.; Jin, Y.; Di, X.; Xu, Z.; Guan, H. Facile Synthesis of Highly Efficient Fluorescent Carbon Dots for Tetracycline Detection. *Environ. Sci. Pollut. Res.* **2020**, *27* (4), 4520–4527. https://doi.org/10.1007/s11356-019-06779-3.

(88) Li, C.; Zeng, C.; Chen, Z.; Jiang, Y.; Yao, H.; Yang, Y.; Wong, W.-T. Luminescent Lanthanide Metal-Organic Framework Test Strip for Immediate Detection of Tetracycline Antibiotics in Water. *J. Hazard. Mater.* **2020**, *384*, 121498. https://doi.org/10.1016/j.jhazmat.2019.121498.

(89) Ahmed, S. R.; Kumar, S.; Ortega, G. A.; Srinivasan, S.; Rajabzadeh, A. R. Target

Specific Aptamer-Induced Self-Assembly of Fluorescent Graphene Quantum Dots on Palladium Nanoparticles for Sensitive Detection of Tetracycline in Raw Milk. *Food Chem.* **2021**, *346*, 128893. https://doi.org/10.1016/j.foodchem.2020.128893.

(90) Starzec, K.; Cristea, C.; Tertis, M.; Feier, B.; Wieczorek, M.; Kościelniak, P.; Kochana, J. Employment of Electrostriction Phenomenon for Label-Free Electrochemical Immunosensing of Tetracycline. *Bioelectrochemistry* **2020**, *132*, 107405. https://doi.org/10.1016/j.bioelechem.2019.107405.

(91) Zhang, Y.; Lv, M.; Gao, P.; Zhang, G.; Shi, L.; Yuan, M.; Shuang, S. The Synthesis of High Bright Silver Nanoclusters with Aggregation-Induced Emission for Detection of Tetracycline. *Sensors Actuators B Chem.* **2021**, *326*, 129009. https://doi.org/10.1016/j.snb.2020.129009.

(92) Liu, Z.; Hou, J.; Wang, X.; Hou, C.; Ji, Z.; He, Q.; Huo, D. A Novel Fluorescence Probe for Rapid and Sensitive Detection of Tetracyclines Residues Based on Silicon Quantum Dots. *Spectrochim. Acta Part A Mol. Biomol. Spectrosc.* **2020**, *240*, 118463. https://doi.org/10.1016/j.saa.2020.118463.

(93) Li, L.; Shi, L.; Jia, J.; Eltayeb, O.; Lu, W.; Tang, Y.; Dong, C.; Shuang, S. Red Fluorescent Carbon Dots for Tetracycline Antibiotics and PH Discrimination from Aggregation-Induced Emission Mechanism. *Sensors Actuators B Chem.* **2021**, *332*, 129513. https://doi.org/10.1016/j.snb.2021.129513.

(94) Wu, W.-J.; Zhao, Q.; Zhou, R.; Liang, Y.-C.; Zhao, W.-B.; Shan, C.-X. Ratiometric Fluorescence Sensor Based on Europium-Grafted ZnO Quantum Dots for Visual and Colorimetric Detection of Tetracycline. *Spectrochim. Acta Part A Mol. Biomol. Spectrosc.* **2021**, *259*, 119901. https://doi.org/10.1016/j.saa.2021.119901.

FOR TABLE OF CONTENTS ONLY